

RESEARCH

Open Access



Utilizing surface-enhanced Raman spectroscopy for the adjunctive diagnosis of osteoporosis

Weihsang Yang^{1†}, Shuang Xia^{1†}, Xu Jia^{2†}, Yuwei Zhu³, Liang Li¹, Cheng Jiang², Hongjian Ji^{2*} and Fengchao Shi^{1*}

Abstract

Osteoporosis (OP) is a chronic disease characterized by diminished bone mass and structural deterioration, ultimately leading to compromised bone strength and an increased risk of fractures. Diagnosis primarily relies on medical imaging findings and clinical symptoms. This study aims to explore an adjunctive diagnostic technique for OP based on surface-enhanced Raman scattering (SERS). Serum SERS spectra from the normal, low bone density, and osteoporosis groups were analyzed to discern OP-related expression profiles. This study utilized partial least squares (PLS) and support vector machine (SVM) algorithms to establish an OP diagnostic model. The combination of Raman peak assignments and spectral difference analysis reflected biochemical changes associated with OP, including amino acids, carbohydrates, and collagen. Using the PLS-SVM approach, sensitivity, specificity, and accuracy for screening OP were determined to be 77.78%, 100%, and 88.24%, respectively. This study demonstrates the substantial potential of SERS as an adjunctive diagnostic technology for OP.

Keywords Surface-enhanced Raman scattering, Osteoporosis, Low bone density, Serum, Silver nanoparticles

Introduction

OP is a gender- and age-related condition characterized by reduced bone mass and structural deterioration, ultimately leading to compromised bone strength and an increased risk of fractures [1, 2]. Among these, hip, spine, and wrist fractures are the most common, and with the ongoing global aging process, the annual number of

individuals disabled or even deceased as a result of these fractures is progressively rising. This poses a significant threat to people's health, imposing substantial economic burdens on individuals, families, and society as a whole [3–5]. Therefore, early diagnosis of OP is imperative. Currently, diagnosis and clinical efficacy assessment of OP primarily rely on clinical symptoms (such as fragility fractures) and medical imaging findings (including dual-energy X-ray absorptiometry, quantitative computed tomography, and quantitative ultrasound) [6–8]. Nevertheless, early-stage OP often lacks overt clinical symptoms. The radiation exposure associated with dual-energy X-ray and quantitative CT imaging poses some adverse effects on human health [9], and the cost of these examinations is substantial, making them unsuitable for large-scale screening. Quantitative ultrasound, while advantageous for its radiation-free and simple operational features, is limited in clinical application due to the absence of standardized technical parameters and

[†]Weihsang Yang, Shuang Xia and Xu Jia have authors contributed equally to this work.

*Correspondence:

Hongjian Ji
hongjianji2006@163.com
Fengchao Shi
shifengchao1980@126.com

¹ Orthopedics Department, Affiliated Hospital 6 of Nantong University, Yancheng 224001, China

² College of Pharmacy, Jiangsu Vocational College of Medicine, Yancheng 224005, China

³ Orthopedics Department, Suzhou BOE Hospital, Suzhou 215000, China



measurement sites [10]. Hence, there is a necessity to explore an early, radiation-free, and cost-effective detection approach for osteoporosis.

Raman spectroscopy, recognized as a versatile and non-invasive diagnostic tool, offers a chemical fingerprint for molecular identification [11]. Its capability to provide molecular-specific information with ultrahigh sensitivity under physiological conditions makes it a valuable technology [12]. Researchers, such as Paschalis, Gamsjaeger, and others, have demonstrated that Raman spectroscopy can furnish both quantitative and qualitative insights into bone mineral and the organic matrix, facilitating the evaluation of bone quality and strength [13, 14]. Caraher and team successfully utilized Raman spectroscopy to predict correlations among bone collagen, keratin, and bone loss induced by estrogen deficiency [15]. Furthermore, Raman spectroscopy has found application in assessing the efficacy of drug treatments for osteoporosis [16–18]. These findings collectively emphasize the promising role of Raman spectroscopy in aiding the diagnosis of OP and evaluating clinical effectiveness. Nevertheless, the prevalent utilization of biological samples in Raman spectroscopy studies currently depends largely on bone tissue biopsies, presenting challenges in sample acquisition. Furthermore, the use of nails as a detection sample may not be universally applicable, restricting its suitability across diverse population groups. This limitation hinders the broad integration of Raman spectroscopy as an innovative diagnostic and analytical tool in diverse clinical scenarios. Therefore, there is an imperative to identify easily accessible tissues with compositional correlations to bone tissue for indirect Raman measurements of bone quality.

Blood detection technologies find extensive application in clinical contexts, and Raman spectroscopy for serum analysis is also widely utilized for the detection of various diseases, such as lung cancer [19], prostate cancer [20, 21], thyroid nodules [22], hepatitis [23], among others. Considering that blood serves as a primary site for the direct release of most bone metabolism products, Raman spectroscopy provides a label-free and non-destructive means of measuring substance information in the blood. Despite the wide application of Raman spectroscopy, there is currently limited exploration of its use in osteoporosis-related research, particularly in serum analysis. Consequently, this study aims to assess the feasibility of early osteoporosis screening through Raman spectroscopy by analyzing serum samples. Nevertheless, traditional serum Raman spectroscopy encounters challenges arising from the extremely small Raman scattering cross-section of molecules, leading to notably weak Raman signals that can be easily overshadowed by fluorescence. This limitation has, to some extent, constrained the

broader application of Raman spectroscopy [24]. Upon adsorption of the analyte onto the surface of nanostructured noble metals, such as Ag or Au, the Raman signals of molecules undergo significant enhancement, concurrently mitigating the background fluorescence effectively. This phenomenon is commonly denoted as SERS [25, 26, 33]. SERS demonstrates outstanding sensitivity, enabling the detection of individual molecules [24]. Presently, SERS technology has been utilized for supplementary diagnostics in osteosarcoma and osteoarthritis [26–28]. Additionally, it has been employed to differentiate the differentiation status of bone marrow mesenchymal stem cells [29].

These investigations validate the encouraging potential of serum SERS in aiding OP diagnosis. The objective of this study is to investigate the viability of early osteoporosis screening using serum SERS technology, utilizing multivariate statistical algorithms, including PLS and SVM. Initial endeavors have been undertaken to compile a dataset of Raman spectral waveforms associated with osteoporosis. We anticipate that this research will establish a fundamental basis for subsequent studies applying spectral diagnostic techniques to OP.

Materials and methods

Participants

The investigation recruited individuals receiving orthopedic care at the Sixth People's Hospital Affiliated with Nantong University between August 2022 and November 2023. Eligible participants were aged between 50 and 90 years and required bone density assessments. Exclusion criteria included: 1) Endocrine and metabolic disorders unrelated to osteoporosis, such as diabetes, thyroid diseases, malignant tumors, etc.; 2) Secondary osteoporosis; 3) Prolonged use of medications potentially impacting skeletal metabolism (e.g., corticosteroids, thyroid hormones, thiazide diuretics, or antiretroviral drugs). The final cohort comprised 66 subjects, classified into groups based on bone density measurements: Normal control group (20 cases), Low bone density group (22 cases), and Osteoporosis group (24 cases). Blood samples were obtained from surplus blood collected during routine biochemical testing, without additional blood withdrawal or associated medical expenses for the participants. Ethical approval was secured from the Ethics Committee of the Sixth People's Hospital Affiliated with Nantong University, with the exemption from obtaining informed consent due to the use of surplus clinical samples. Following approval of the research protocol, the sample collection phase commenced.

Sample preparation

Blood samples were procured from the participants between August 2022 and November 2023. Employing the prescribed biochemical sample collection protocol, 5 mL of blood was obtained in anticoagulant tubes and allowed to undergo standing. Subsequently, the samples underwent centrifugation (4 °C, 4000 rpm, 10 min) to facilitate biochemical analysis. Following the completion of the biochemical analysis, centrifugation was performed again with the same parameters. Thereafter, 200 mL of the resultant supernatant was carefully pipetted into a 500 µL cryovial. The cryovials, duly labeled with their respective groups, were sealed and then stored in a −80 °C freezer for subsequent measurements.

Coffee ring effect and serum SERS measurements

Following Leopold's method, the resulting silver colloid exhibited a milky gray color [30, 31]. For detailed preparation methods, please refer to the attachment. Figure 1A illustrates the transmission electron microscopy (TEM) image of silver nanoparticles (AgNPs). Figure 1B shows the maximum ultraviolet–visible extinction of the silver colloids at 412 nm. Then, we established a SERS substrate utilizing the coffee ring effect of immobilized droplets. Prior to SERS measurements, 20 µL of each serum sample from the normal, low bone density, and osteoporosis groups was individually mixed with an equivalent volume of concentrated silver sol. Subsequently, 40 µL of the resulting mixture was dropped onto a glass slide and allowed to dry naturally at room temperature (25 °C) for 40 min. Finally, a prominent "coffee ring" containing

a substantial amount of AgNPs formed at the periphery of the sample. Aggregated AgNPs or clusters within the coffee ring region generated numerous "hotspots," effectively enhancing the Raman signals.

Using a Thermo Scientific DXR3 Raman spectrometer, the serum SERS signals were obtained in the wave-number of 400–1800 cm^{-1} with 30 s integration time. A 532 nm diode laser was focused on the coffee ring region to stimulate samples through an MPLan 10× objective (numerical aperture: 0.25). The laser spot size focused on the sample was approximately 2.1 µm, with a laser power of 0.1 mW and an estimated spectral resolution ranging from 5.5 to 8.3 cm^{-1} . The WIRE 3.4 software (Renishaw) was used to realize signal collection.

Data processing and analysis

By scanning the Raman spectra of the slides and subtracting them from each sample's spectral data, we reduced background fluorescence interference [32]. Then, using the second derivative, we identified baseline anchor points for baseline calibration and applied the Savitzky–Golay method for smoothing. Before applying machine learning, Z-score normalization was performed on all data to mitigate intensity variations caused by laser power fluctuations, ensuring a more accurate analysis of serum SERS signals [33]. The Raman signals representing each sample were acquired by randomly scanning the coffee ring area of the samples. These signals serve as a representation of individual samples. Ultimately, each sample group, including the normal, low bone density,

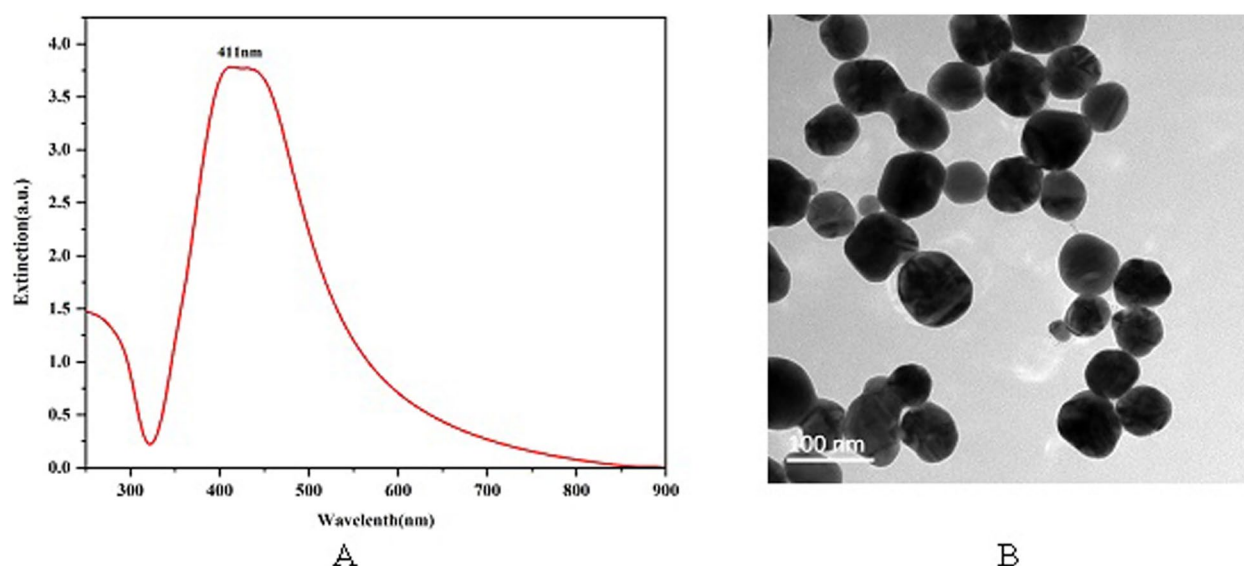


Fig. 1 **A** UV–VIS absorption of silver colloids. **B** the inserted picture is the TEM image of AgNPs

and osteoporosis groups, encompassed multiple SERS spectra for subsequent data analysis.

Statistical analysis of clinical data was performed using SPSS 27.0 software. Continuous data were expressed as mean \pm standard deviation ($\bar{x} \pm s$), and intergroup comparisons were conducted using analysis of variance (ANOVA). Categorical data were presented as composition ratios, and intergroup comparisons were assessed using the chi-square test. All statistical tests were two-tailed, and a significance level of $P < 0.05$ was considered indicative of statistically significant differences.

In order to investigate the feasibility of SERS in diagnosing OP, PLS and SVM algorithms were introduced to establish the diagnostic model for SERS data discrimination [34, 35]. In this study, data analysis of the dataset was conducted using the scikit-learn module in Python 3.11, specifically employing PLS and SVM techniques. The primary goal was to reduce the dimensionality of the spectral data and generate a set of new latent variables (PLS components). Subsequently, the optimal number of components for PLS was determined through cross-validation and estimation of mean squared prediction error (MSPE). This approach aimed to avoid overfitting of the diagnostic model by preventing an excessive number of PLS components. Subsequently, the selected PLS components were integrated into the SVM algorithm. The SVM was employed to calculate the sensitivity, specificity, and accuracy of sample classification. Further assessment of diagnostic outcomes was conducted through the use of a confusion matrix and receiver operating characteristic (ROC) curves.

Results

Clinical features

Significant differences were observed in the gender and age distribution among the three study groups, while no statistically significant differences were found in parameters, such as body mass index (BMI), liver function, and kidney function. The percentages of females in the NG (Normal Group), LBD (Low Bone Density) group,

and OP group were 60.0%, 63.64%, and 100.00%, respectively. The age distribution values in the NG, LBD group, and OP group were (57.65 ± 6.82), (69.59 ± 9.89), and (74.25 ± 7.22), respectively. Detailed results are presented in Table 1. In order to illustrate that the discrepancies observed in Raman spectra among the groups are not influenced by differences in age and gender, we generated spectra for distinct age groups (≤ 60 and > 60) as well as for different genders, as depicted in Supplementary Fig. 1. These analyses revealed no discernible differences.

Enhancement effect and stability of serum SERS detection based on coffee ring effect

The mixture of serum/AgNPs dripping onto the glass slide could form a “coffee ring” because it was not simply evaporated and naturally dried at the dripping place. As the mixture began to dry, it actually created its own outward motion, drawing the AgNPs inside of the mixture toward to the edges [26]. In Fig. 2A, the SERS spectra recorded from both the coffee ring area (Region I) and the central region (Region II) of a representative sample within the normal group are presented. The comparison of the intensities of 12 major SERS peaks obtained from these two regions is illustrated in Fig. 2B. As depicted in the preceding figures, it is apparent that the SERS intensity obtained from the coffee ring area (Region I) is notably amplified in comparison to the signals gathered from the central region. Ensuring the stability and reproducibility of SERS signals is paramount for subsequent spectral analysis. To assess the stability of the serum SERS signal amplification within the coffee ring, we randomly recorded 5 SERS spectra from different positions within the same sample's coffee ring area, as illustrated in Fig. 2C. In comparison to the blue dashed line representing the Raman signals from the central region, the five SERS signals collected randomly from the coffee ring region generally exhibited higher intensities. This observation indicates a significant enhancement in Raman signal strength through the utilization of the coffee ring

Table 1 Comparison of general data between groups

Project	NG(20)	LBD(22)	OP(24)	F/ χ^2	P
Sex(male /female)	8 (40.00%)/12 (60.00%)	8 (36.36%)/14 (63.64%)	0 (0.00%)/24 (100.00%)	12.144	0.002
Age	57.65 ± 6.82	69.59 ± 9.89	74.25 ± 7.22	23.800	< 0.001
BMI($< 30/ \geq 30$)	1.10 ± 0.31	1.00 ± 0.00	1.17 ± 0.38	1.971	0.148
Uric acid(normal/abnormal)	1.30 ± 0.47	1.36 ± 0.49	1.21 ± 0.41	0.668	0.516
Creatinine(normal/abnormal)	1.20 ± 0.41	1.41 ± 0.50	1.25 ± 0.44	1.239	0.297
ALT(normal/abnormal)	1.15 ± 0.37	1.09 ± 0.29	1.17 ± 0.38	0.291	0.748
AST(normal/abnormal)	1.05 ± 0.22	1.05 ± 0.21	1.17 ± 0.38	1.303	0.279

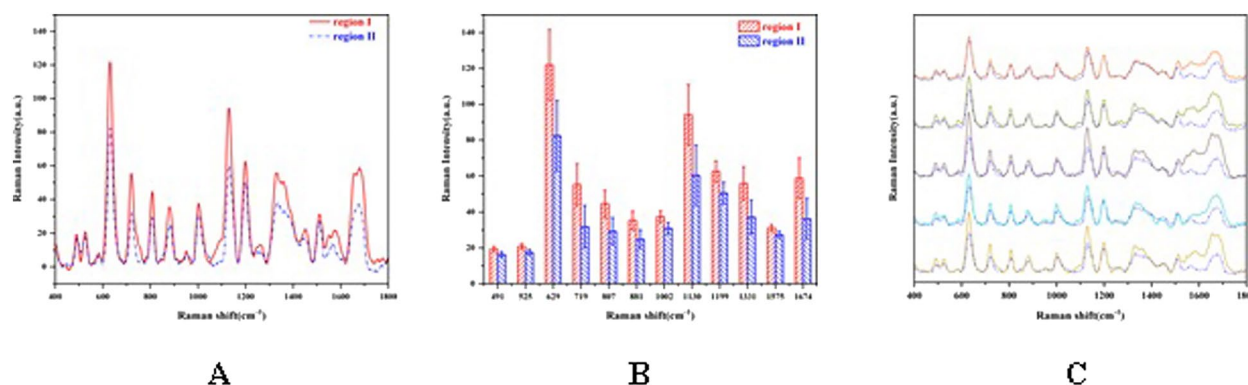


Fig. 2 The enhancement effect and stability of SERS signals obtained from the coffee ring region. **A** SERS signals from the coffee ring region and central position of the same serum sample. **B** Comparison of the intensity of the main SERS peaks in the spectra measured from the coffee ring region and central position. **C** Comparison of SERS signals obtained from five randomly selected positions within the coffee ring region with those from the central region

effect, demonstrating good stability. Therefore, this method proves beneficial for high-sensitivity SERS detection and reliable analysis of serum biochemical components.

Comparison and analysis of serum SERS signal

Figure 3A depicts the average SERS spectra and standard deviations within the range of 400–1800 cm^{-1} for three groups: NG ($n=20$), LBD group ($n=22$), and OP group ($n=24$). The solid line and the shaded region correspond to the mean SERS spectra and the standard deviation, respectively. Furthermore, the spectral disparities among the NG, LBD group, and OP group are vividly illustrated in the Fig. 3B–D. Notably, significant variations in the spectra are evident within the spectral ranges of 490–670 cm^{-1} , 1100–1400 cm^{-1} , and 1470–1760 cm^{-1} (highlighted in yellow). The observed alterations are predominantly linked to variations in amino acids, carbohydrates, and collagen. In summary, noticeable distinctions exist in the SERS spectra among the three sample groups. As a result, these distinctive spectral features can be employed for the purpose of distinguishing and screening individuals with osteoporosis. Some SERS bands exhibit narrow peaks in the spectra, likely attributed to the vibrations of specific functional groups or chemical bonds within the molecules. A comprehensive compilation of the primary peaks observed in serum SERS, alongside their assignments, is presented in Table 2. These assignments are derived from insights gathered from diverse research reports [33, 36, 37].

OP screening based on serum SERS combined with multivariate statistical analysis

The SERS spectra across different sample groups exhibited similarities, making it challenging to distinguish samples through direct observation. Therefore, a robust and effective multivariate statistical approach was introduced for the analysis and extraction of spectral diagnostic information, specifically for OP screening. In this study, the PLS-SVM method was employed to extract diagnostically relevant SERS features for OP diagnosis. Initially, the PLS method was applied to reduce the dimensionality of the SERS data. The optimal number of PLS components was determined through a grid search combined with the method of MSPE. As depicted in Fig. 4A, the MSPE curve generated by PLS exhibited a rapid initial decline followed by a slower descent as the number of components increased. Based on the grid search results, the optimal number of PLS components was determined to be 6. Figure 4B shows the contribution rates of the PLS components generated by the PLS algorithm. When there are 6 PLS components, the contribution rate to the model prediction approaches 90%. Figure 4C exhibits the average loadings of the initial six components in PLS, elucidating the influence of each wavenumber on the separation. Eventually, these 6 features obtained after PLS dimensionality reduction were input into the SVM algorithm for subsequent identification and screening of OP.

In this investigation, grid search analysis applied to the SVM model revealed that a linear kernel demonstrated optimal classification performance. Consequently, the SVM algorithm with a linear kernel was employed for sample classification. In order to elucidate the unique characteristics of the Raman spectra and investigate differences at a granular level, posterior probability scatter

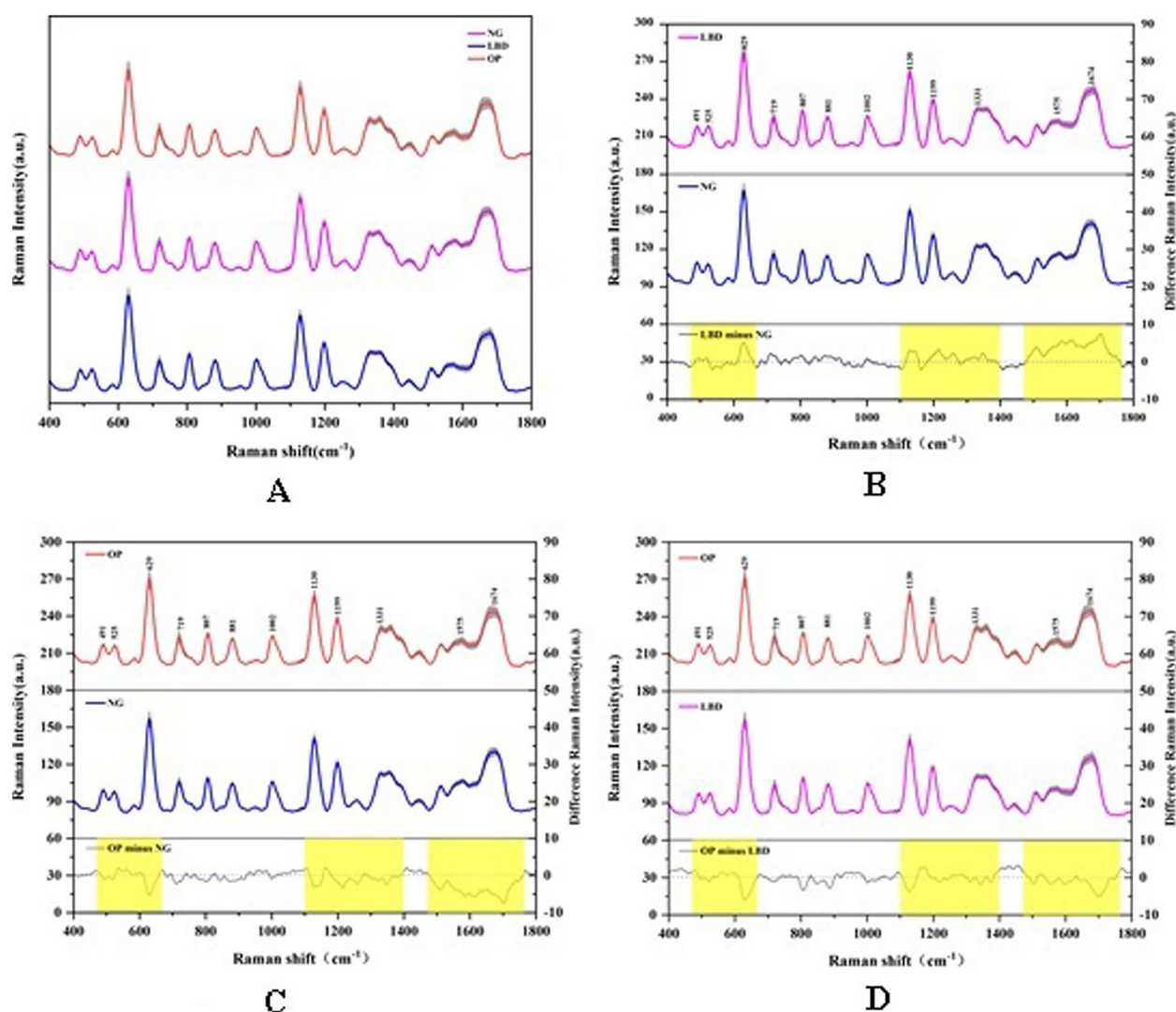


Fig. 3 Comparison of serum SERS spectra. **A** average SERS spectra of serum samples belonging to the NG, LBD group, and OP group. The shaded areas represent standard deviations (SD). **B C D** illustrate spectra differences among the NG (blue solid line), LBD group (purple solid line), and OP group (red solid line). Spectral differences between the two groups are indicated by black solid lines, with significant changes highlighted in yellow for emphasis

plots were generated. Illustrated in Fig. 5A, this plot was crafted to assess the model's confidence across various classification outcomes. As illustrated in the figure, the misclassification of three blood samples by the PLS-SVM model is evident, comprising two cases from the OP group, and the remaining one cases from the NG. Figure 5B illustrates the confusion matrices for the three sets of sample test data obtained using the optimal classifier. The classification outcomes are presented in Table 3, detailing sensitivity, specificity, and accuracy for OP screening as 77.78%, 100%, and 88.24%, respectively. Furthermore, the introduction of the ROC curve provided additional validation for the OP screening efficacy of this

study. As depicted in Fig. 5C, the ROC curve areas under the curve (AUC) for the NG, LBD group, and the OP group were 1.000, 1.000, and 0.972, respectively. These findings underscore the significant potential of integrating SERS technology with the PLS-SVM diagnostic algorithm for osteoporosis screening.

Discussion

Osteoporosis is a common chronic condition influenced by factors, such as age and gender. The global increase in the aging population has led to a rising incidence of osteoporosis [38]. Currently, there is a notable absence of convenient and cost-effective screening methods for this

Table 2 Peak positions and assignment of serum SERS bands

Peak positions (cm ⁻¹)	Tentative assignments
491	L-arginine: ring vibration
525	Cholesterol ester
629	Tyrosine: C–S stretching vibration
719	Adenine, coenzyme A
807	Glutathione: C–C–O stretching vibration
881	Glutathione: C–O–H bending vibration
1002	Phenylalanine: Ring breathing
1130	D-mannose: C–N stretching vibration
1199	Amide III, CH ₂ wagging vibrations from glycine backbone
1331	CH ₂ CH ₂ wagging mode of collagen; Nucleic acid bases
1575	Ring breathing modes in the DNA bases
1674	Amide I

condition. Often, osteoporosis is identified only when patients seek medical attention due to pain or fractures, placing a substantial economic burden on individuals, families, and society. The serum SERS technology improves Raman signal responses utilizing silver sol, effectively suppressing background fluorescence, and minimizing extraneous noise interference [33, 39]. Furthermore, the mechanism involves particle capture at the liquid–gas interface and the natural evaporation process during drying [40, 41], leading to the development of a ring-shaped "coffee ring" at the outer edge of the mixed solution containing silver sol and serum. This ring concentrates AgNPs, considerably enhancing the molecular Raman scattering signals and enabling highly sensitive SERS detection.

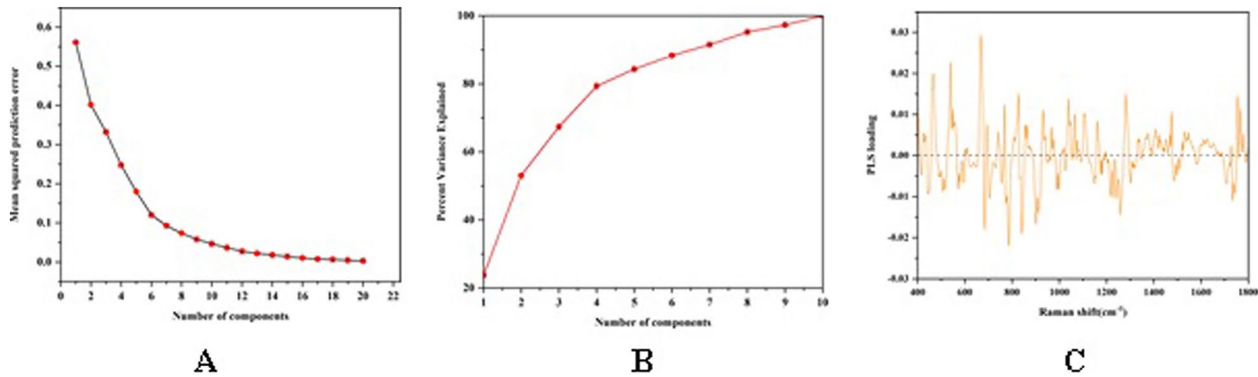


Fig. 4 Reducing dimensionality of spectra data using the partial least Squares method. **A** Performance evaluation of the Predictive Mean Squared Error generated by the PLS algorithm. The MSE curve generated by PLS exhibited a rapid initial decline followed by a slower descent as the number of components increased. Based on the grid search results, the optimal number of PLS components was determined to be 6. **B** The contribution rate PLS components. When there are 6 PLS components, the contribution rate to the model prediction approaches 90%. **C** The average loading of the initial six components in PLS, elucidating the influence of each wavenumber on the separation

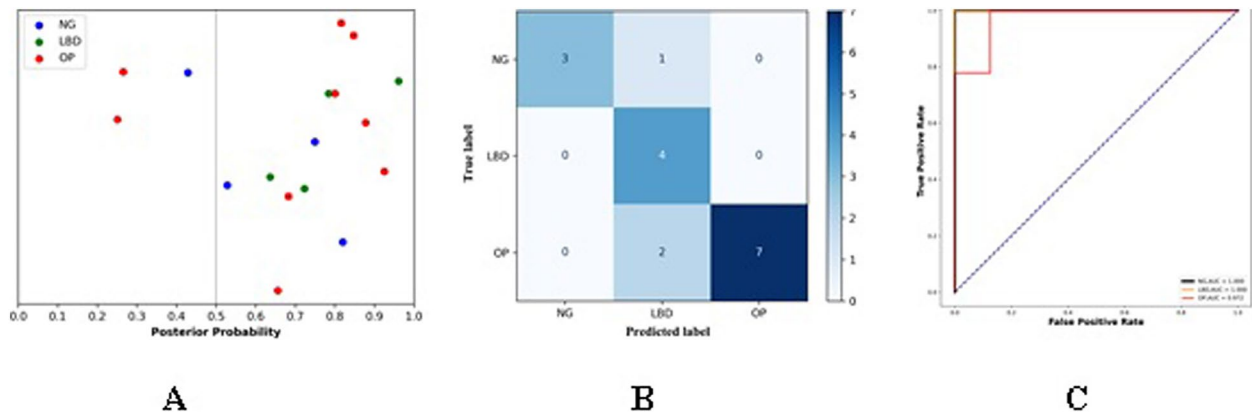


Fig. 5 Performance evaluation of the PLS-SVM-based screening of OP. **A** posterior probability plot of the test set (blue circles: NG; green circle: LBD group; red circles: OP group). **B** Confusion matrices of classification results for different sample test sets. **C** Receiver Operating Characteristic curve for classification results of different samples, with Area Under Curve value of 1 for the NG and LBD group, and 0.972 for the OP group

Table 3 Classification results of the PLS-SVM method using tenfold cross-validation

Identification of sample groups	Sensitivity	Specificity	Accuracy
NG	75%	100%	94.12%
LBD	100%	76.92%	82.35%
OP	77.78%	100%	88.24%

The main peaks in the Raman spectra are assigned in Table 2. The highlighted yellow regions in Fig. 3 illustrate additional spectral distinctions among the three serum sample groups. Specifically, the osteoporosis group displays diminished levels of L-arginine, Tyrosine, D-mannose, Amide III, I, as well as collagen and DNA bases, resulting in corresponding Raman bands at 491, 629, 1130, 1199, 1331, 1575, and 1674 cm^{-1} , respectively. Numerous studies have suggested that L-arginine could effectively mitigate bone loss [42, 43], with its primary mechanism potentially linked to the increased production of nitric oxide and the synthesis of Type I collagen by osteoblasts in both normal and osteoporotic bones [44]. Additionally, mannose components present in various natural herbs have been shown to effectively suppress bone resorption, thereby exerting an anti-osteoporotic effect [45, 46], as demonstrated in animal experiments [47]. Silva et al. performed a chemical composition analysis of the femoral neck region in postmenopausal female rats using Raman spectroscopy. They observed that, in comparison to OP rats, the trained group exhibited higher spectral curves in phosphate, Amide I, Amide III, and collagen content [48]. This observation is consistent with the findings obtained from our SERS scans of patient serum, wherein the Amide III and Amide I peaks at 1199 and 1674 cm^{-1} , along with collagen at 1331 cm^{-1} , were significantly lower in the OP group when compared to the normal group. Simultaneously, the OP group exhibited elevated levels of cholesterol lipids at 525 cm^{-1} . Experiments conducted by Marco et al. suggest a negative correlation between cholesterol and 25(OH)D levels, with low levels of 25(OH)D being identified as a significant contributing factor to the onset of OP [49]. Opinions on the role of Tyrosine levels in predicting OP are not unanimously agreed upon, with some literature presenting completely opposing conclusions [50–52]. In Fig. 3D, the OP group exhibits lower SERS peak intensity attributed to Tyrosine at 629 cm^{-1} , suggesting a potential positive correlation between tyrosine levels and bone density. However, it is worth noting that Fig. 4C indicates a minor contribution of this substance to OP screening. Clinical experiments conducted by Le et al. also revealed no significant correlation between dietary supplementation of aromatic amino acids (tryptophan, phenylalanine,

tyrosine) and bone mineral density (BMD) [53]. In summary, further research is needed to elucidate the role of tyrosine in predicting OP. Moreover, notable disparities in the Raman spectra between the NG and the LBD group, as depicted in Fig. 3B, demonstrate an opposing trend compared to that illustrated in Fig. 3D across various spectral bands. This inverse pattern in the Raman spectra between the NG and the LBD group in different bands may indicate compensatory mechanisms during the progression of OP. Taken together, these results underscore the capability of ultra-sensitive SERS to delineate subtle changes in the biochemical composition of serum in OP patients, suggesting the potential use of these substances as biomarkers for OP screening.

In order to identify individuals with reduced bone density and osteoporosis within the normal population, we employed the PLS-SVM method for the analysis of SERS spectra. The application of PLS facilitated the condensation of high-dimensional spectral data into several PLS components, ensuring the retention of essential sample-specific details. Research suggests that PLS utilizes group affinity information, such as grouping variables, to enhance discrimination among different groups. Therefore, PLS is considered more effective than traditional PCA methods in reducing the dimensionality of spectral data [54]. However, directly utilizing of all PLS components to construct an OP discrimination model may lead to overfitting, impairing the model's ability to predict new samples. To address this issue, the MSPE curve was utilized to identify the optimal number of PLS components [55]. As illustrated in Fig. 4A, the MSPE curve produced by PLS demonstrates an initial steep decline with the increasing number of PLS components, followed by a more gradual descent, eventually stabilizing. Figure 4B demonstrates that when employing six components, the model's contribution to prediction approaches 90%. Although increasing the number of components marginally enhances prediction accuracy, it also elevates the risk of overfitting. Consequently, in this investigation, the first six PLS components were chosen and integrated into the SVM algorithm for effective discrimination of OP cases. Furthermore, Fig. 4C presents the average loadings across these six groups. SVM is a powerful classification algorithm known for its robustness and effectiveness in high-dimensional spaces. It works well even when the number of samples is smaller than the number of features, which is a common scenario in spectral analysis. Compared to deep learning algorithms such as random forest regression, SVM offers advantages, such as a simple model structure and less computational time [56]. Given that the primary objective of this experiment is to validate the feasibility of Raman spectroscopy for early screening of osteoporosis, a simpler and less time-consuming SVM

model was chosen. Combining PLS and SVM leverages the strengths of both methods. PLS is used for dimensionality reduction and feature extraction, reducing the complexity of the input data. The reduced-dimensional data is then classified using SVM, which excels at finding optimal decision boundaries in the reduced feature space. Moreover, in further evaluating diagnostic performance, the posterior probability plot (Fig. 5A) illustrates highly intuitive results. Due to the complexity of OP, influenced by various factors, such as ethnicity, environment, lifestyle, and genetics [57], a few outliers may still appear in the actual diagnostic process of PLS-SVM, making it challenging to entirely eliminate the possibility of misclassifications. In this study, sensitivity, specificity, and diagnostic accuracy for screening OP were determined to be 77.78%, 100%, and 88.24%, respectively. Certainly, this experiment has some limitations. For example, the relatively small sample size may predispose the model to overfitting and diminish its capacity for generalization, potentially yielding excessively optimistic experimental results. Future efforts will prioritize the expansion of the sample size, optimization of experimental procedures, and the exploration of ensemble algorithms, such as random forest, during model construction to improve the diagnostic model's generalization performance. In summary, this experiment underscores the considerable potential of OP screening through the integration of serum SERS detection and the PLS-SVM method. We posit that these findings make valuable contributions to the early screening and supportive diagnosis of OP.

Conclusion

In this study, we successfully obtained high-quality serum SERS spectra from three groups: NG, LBD group, and OP group, utilizing the coffee ring effect. By analyzing the assignments of Raman bands and spectral differences, we demonstrated that SERS could qualitatively and quantitatively compare subtle changes in serum biochemical components between different groups. These changes are indicative of OP-related expression profiles, validating the feasibility of using SERS for this purpose. Furthermore, integrating SERS spectra with the PLS-SVM method enabled effective identification of OP samples, achieving diagnostic sensitivity, specificity, and accuracy of 77.78%, 100%, and 88.24%, respectively.

This study underscores the potential of SERS as an adjunctive diagnostic tool for OP, providing a promising approach for early screening and diagnosis. The findings suggest that SERS can complement traditional diagnostic methods, offering a non-invasive, sensitive, and specific alternative. Future research should focus on expanding the sample size, optimizing the SERS protocol, and validating these findings in larger clinical trials. Additionally,

further exploration into the biochemical mechanisms underlying the observed spectral changes will enhance our understanding and application of SERS in OP diagnostics.

Supplementary Information

The online version contains supplementary material available at <https://doi.org/10.1186/s40001-024-02081-2>.

Supplementary materials 1.

Author contributions

Conceptualization: Weihang Yang. Formal analysis: Shuang Xia Funding acquisition: Hongjian Ji and Fengchao Shi. Investigation: Weihang Yang, Cheng Jiang and Jia Xu. Project administration: Fengchao Shi. Validation: Hongjian Ji and Shuang Xia. Visualization: Weihang Yang and Liang Li. Writing—original draft: Weihang Yang and Hongjian Ji. Writing—review & editing: Weihang Yang and Yuwei Zhu.

Funding

This work was supported by funding from Jiangsu Provincial Commission of Health and Family Planning (No.QNRC2016465), Yancheng Health Commission (No.YK2023099), Nantong University Clinical Medicine Special Project (No.2023JZ027) and Jiangsu Vocational College of Medicine High-level Talent Program (No.20226102).

Availability of data and materials

Data is provided within the manuscript or supplementary information files.

Declarations

Competing interests

The authors declare no competing interests.

Received: 11 May 2024 Accepted: 24 September 2024

Published online: 30 September 2024

References

1. Compston JE, Mcclung MR, Leslie WD. Osteoporosis. *Lancet*. 2019;393(10169):364–76.
2. Ralston SH, Uitterlinden AG. Genetics of osteoporosis. *Endocr Rev*. 2010;31(5):629–62.
3. Harvey N, Dennison E, Cooper C. Osteoporosis: impact on health and economics. *Nat Rev Rheumatol*. 2010;6(2):99–105.
4. Papadimitriou N, Tsilidis KK, Orfanos P, et al. Burden of hip fracture using disability-adjusted life-years: a pooled analysis of prospective cohorts in the CHANCES consortium. *Lancet Public Health*. 2017;2(5):e239–46.
5. Brown C. Osteoporosis: staying strong. *Nature*. 2017;550(7674):S15–7.
6. Qaseem A, Forciea MA, Mclean RM, et al. Treatment of low bone density or osteoporosis to prevent fractures in men and women: a clinical practice guideline update from the American college of physicians. *Ann Intern Med*. 2017;166(11):818–39.
7. Lane NE. Epidemiology, etiology, and diagnosis of osteoporosis. *Am J Obstet Gynecol*. 2006;194(2 Suppl):S3–11.
8. Lane JM, Russell L, Khan SN. Osteoporosis. *Clin Orthop Relat Res*. 2000;372:139–50.
9. Link TM. Osteoporosis imaging: state of the art and advanced imaging. *Radiology*. 2012;263(1):3–17.
10. Roux C, Dougados M. Quantitative ultrasound in postmenopausal osteoporosis. *Curr Opin Rheumatol*. 2000;12(4):336–45.
11. Serebrennikova KV, Berlina AN, Sotnikov DV, et al. Raman scattering-based biosensing: new prospects and opportunities. *Biosensors*. 2021;11(12):512.

12. Tanwar S, Paidi SK, Prasad R, et al. Advancing Raman spectroscopy from research to clinic: translational potential and challenges. *Spectrochim Acta A Mol Biomol Spectrosc*. 2021;260: 119957.
13. Gamsjaeger S, Mendelsohn R, Boskey AL, et al. Vibrational spectroscopic imaging for the evaluation of matrix and mineral chemistry. *Curr Osteoporos Rep*. 2014;12(4):454–64.
14. Paschalis EP, Gamsjaeger S, Klaushofer K. Vibrational spectroscopic techniques to assess bone quality. *Osteoporos Int*. 2017;28(8):2275–91.
15. Caraher MC, Sophocleous A, Beattie JR, et al. Raman spectroscopy predicts the link between claw keratin and bone collagen structure in a rodent model of oestrogen deficiency. *Biochim Biophys Acta*. 2018;1864(2):398–406.
16. Bohic S, Rey C, Legrand A, et al. Characterization of the trabecular rat bone mineral: effect of ovariectomy and bisphosphonate treatment. *Bone*. 2000;26(4):341–8.
17. Paschalis EP, Gamsjaeger S, Hassler N, et al. Vitamin D and calcium supplementation for three years in postmenopausal osteoporosis significantly alters bone mineral and organic matrix quality. *Bone*. 2017;95:41–6.
18. Hofstetter B, Gamsjaeger S, Phipps RJ, et al. Effects of alendronate and risedronate on bone material properties in actively forming trabecular bone surfaces. *J Bone Mineral Res*. 2012;27(5):995–1003.
19. Cao D, Lin H, Liu Z, et al. Serum-based surface-enhanced Raman spectroscopy combined with PCA-RCKNCN for rapid and accurate identification of lung cancer. *Anal Chim Acta*. 2022;1236: 340574.
20. Chen N, Rong M, Shao X, et al. Surface-enhanced Raman spectroscopy of serum accurately detects prostate cancer in patients with prostate-specific antigen levels of 4–10 ng/mL. *Int J Nanomed*. 2017;12:5399–407.
21. Shao X, Pan J, Wang Y, et al. Evaluation of expressed prostatic secretion and serum using surface-enhanced Raman spectroscopy for the noninvasive detection of prostate cancer, a preliminary study. *Nanomedicine*. 2017;13(3):1051–9.
22. Xia L, Lu J, Chen Z, et al. Identifying benign and malignant thyroid nodules based on blood serum surface-enhanced Raman spectroscopy. *Nanomedicine*. 2021;32: 102328.
23. Gao F, Lu D-C, Zheng T-L, et al. Fully connected neural network-based serum surface-enhanced Raman spectroscopy accurately identifies non-alcoholic steatohepatitis. *Hepatol Int*. 2023;17(2):339–49.
24. Feng S, Zheng Z, Xu Y, et al. A noninvasive cancer detection strategy based on gold nanoparticle surface-enhanced Raman spectroscopy of urinary modified nucleosides isolated by affinity chromatography. *Biosens Bioelectron*. 2017;91:616–22.
25. Mosier-Boss PA. Review of SERS Substrates for Chemical Sensing. *Nanomaterials*. 2017;7(6):142.
26. Yu Y, Chen W, Wang L, et al. An auxiliary diagnostic technology and clinical efficacy evaluation in knee osteoarthritis based on serum surface-enhanced Raman spectroscopy. *Spectrochim Acta A Mol Biomol Spectrosc*. 2023;296: 122654.
27. Yue J, Liu Z, Cai X, et al. Bull serum albumin coated Au@Ag nanorods as SERS probes for ultrasensitive osteosarcoma cell detection. *Talanta*. 2016;150:503–9.
28. Chakraborty A, Das A, Raha S, et al. Size-dependent apoptotic activity of gold nanoparticles on osteosarcoma cells correlated with SERS signal. *J Photochem Photobiol B*. 2020;203: 111778.
29. Cao X, Shan Y, Tan L, et al. Hollow Au nanoflower substrates for identification and discrimination of the differentiation of bone marrow mesenchymal stem cells by surface-enhanced Raman spectroscopy. *J Mater Chem B*. 2017;5(30):5983–95.
30. Leopold N, Bernhard L. A new method for fast preparation of highly surface-enhanced Raman scattering (SERS) active silver colloids at room temperature by reduction of silver nitrate with hydroxylamine hydrochloride. *J Phys Chem B*. 2003;107:5723–7.
31. Guo Q, Peng Y, Chao K. Raman enhancement effect of different silver nanoparticles on salbutamol. *Heliyon*. 2022;8(6): e09576.
32. Zhao J, Lui H, Mclean DJ, et al. Automated autofluorescence background subtraction algorithm for biomedical Raman spectroscopy. *Appl Spectrosc*. 2007;61(11):1225–32.
33. Feng S, Chen R, Lin J, et al. Nasopharyngeal cancer detection based on blood plasma surface-enhanced Raman spectroscopy and multivariate analysis. *Biosens Bioelectron*. 2010;25(11):2414–9.
34. Li X, Yang T, Li S, et al. Noninvasive liver diseases detection based on serum surface enhanced Raman spectroscopy and statistical analysis. *Opt Express*. 2015;23(14):18361–72.
35. Gao S, Lin Y, Zhao X, et al. Label-free surface enhanced Raman spectroscopy analysis of blood serum via coffee ring effect for accurate diagnosis of cancers. *Spectrochim Acta A Mol Biomol Spectrosc*. 2022;267(Pt 2): 120605.
36. Wu Q, Qiu S, Yu Y, et al. Assessment of the radiotherapy effect for nasopharyngeal cancer using plasma surface-enhanced Raman spectroscopy technology. *Biomed Opt Express*. 2018;9(7):3413–23.
37. Shakeel S, Nawaz H, Majeed MI, et al. Surface-enhanced Raman spectroscopic analysis of centrifugally filtered blood serum samples of hepatitis C patients. *Photodiagnosis Photodyn Ther*. 2022;39: 102949.
38. Riggs BL, Melton LJ. The worldwide problem of osteoporosis: insights afforded by epidemiology. *Bone*. 1995;17(5 Suppl):505S–511S.
39. Srivastava I, Xue R, Jones J, et al. Biomimetic surface-enhanced Raman scattering nanoparticles with improved dispersibility, signal brightness, and tumor targeting functions. *ACS Nano*. 2022;16(5):8051–63.
40. Liamsau V, Fan C, Liu G, et al. Speciation of thioarsenicals through application of coffee ring effect on gold nanofilm and surface-enhanced Raman spectroscopy. *Anal Chim Acta*. 2020;1106:88–95.
41. Jafari Kang S, Vandadi V, Felske JD, et al. Alternative mechanism for coffee-ring deposition based on active role of free surface. *Phys Rev E*. 2016;94(6–1): 063104.
42. Jennings A, Macgregor A, Spector T, et al. Amino acid intakes are associated with bone mineral density and prevalence of low bone mass in women: evidence from discordant monozygotic twins. *J Bone Mineral Res*. 2016;31(2):326–35.
43. Cao S, Li Y, Song R, et al. L-arginine metabolism inhibits arthritis and inflammatory bone loss. *Ann Rheum Dis*. 2023;83(1):72–87.
44. Fini M, Torricelli P, Giavaresi G, et al. Effect of L-lysine and L-arginine on primary osteoblast cultures from normal and osteopenic rats. *Biomed Pharmacothera = Biomed Pharmacother*. 2001;55(4):213–20.
45. Lin B, Deng X, Xu P, et al. Structural characterization and anti-osteoporosis effect of an arabinomannan from *Anemarrhena asphodeloides* Bge. *Int J Biol Macromol*. 2023;231: 123324.
46. Sun X, Wei B, Peng Z, et al. Protective effects of *dipsacus asper* polysaccharide on osteoporosis in vivo by regulating RANKL/RANK/OPG/VEGF and PI3K/Akt/eNOS pathway. *Int J Biol Macromol*. 2019;129:579–87.
47. Liu H, Gu R, Zhu Y, et al. D-mannose attenuates bone loss in mice via Treg cell proliferation and gut microbiota-dependent anti-inflammatory effects. *Therap Adv Chronic Dis*. 2020;11:2040622320912661.
48. Dos Santos SRA, Peres-Ueno MJ, Nicola AC, et al. The microarchitecture and chemical composition of the femur neck of senescent female rats after different physical training protocols. *Geroscience*. 2023. <https://doi.org/10.1007/s11357-023-00948-6>.
49. Cutillas-Marco E, Prosper AF, Grant WB, et al. Vitamin D status and hypercholesterolemia in Spanish general population. *Dermatoendocrinol*. 2013;5(3):358–62.
50. Cui Z, Feng H, He B, et al. Relationship between serum amino acid levels and bone mineral density: a mendelian randomization study. *Front Endocrinol*. 2021;12: 763538.
51. Palacios-González B, Ramírez-Salazar EG, Rivera-Paredes B, et al. A multi-omic analysis for low bone mineral density in postmenopausal women suggests a relationship between diet, metabolites, and microbiota. *Microorganisms*. 2020;8(11):1630.
52. Pontes TA, Barbosa AD, Silva RD, et al. Osteopenia-osteoporosis discrimination in postmenopausal women by ¹H NMR-based metabolomics. *PLoS ONE*. 2019;14(5): e0217348.
53. Le B, Bůžková P, Robbins JA, et al. The association of aromatic amino acids with incident hip fracture, aBMD, and body composition from the cardiovascular health study. *Calcif Tissue Int*. 2019;105(2):161–72.
54. Yu Y, Lin Y, Xu C, et al. Label-free detection of nasopharyngeal and liver cancer using surface-enhanced Raman spectroscopy and partial least squares combined with support vector machine. *Biomed Opt Express*. 2018;9(12):6053–66.
55. Ma Y, Chi J, Zheng Z, et al. Therapeutic prognosis of prostate cancer using surface-enhanced Raman scattering of patient urine and multivariate statistical analysis. *J Biophotonics*. 2021;14(1): e202000275.
56. Reel PS, Reel S, Pearson E, et al. Using machine learning approaches for multi-omics data analysis: a review. *Biotechnol Adv*. 2021;49: 107739.

57. Licata AA. Prevention and osteoporosis management. *Cleve Clin J Med*. 1994;61(6):451–60.

Publisher's Note

Springer Nature remains neutral with regard to jurisdictional claims in published maps and institutional affiliations.